IOPscience iopscience.iop.org

Home Search Collections Journals About Contact us My IOPscience

One-, two-and three-dimensional nanostructures with atom lithography

This article has been downloaded from IOPscience. Please scroll down to see the full text article.

2003 J. Phys.: Condens. Matter 15 R233

(http://iopscience.iop.org/0953-8984/15/6/201)

View the table of contents for this issue, or go to the journal homepage for more

Download details:
IP Address: 171.66.16.119
The article was downloaded on 19/05/2010 at 06:33

Please note that terms and conditions apply.

INSTITUTE OF PHYSICS PUBLISHING JOURNAL OF PHYSICS: CONDENSED MATTER

J. Phys.: Condens. Matter **15** (2003) R233–R255 PII: S0953-8984(03)57397-0

TOPICAL REVIEW

One-, two- and three-dimensional nanostructures with atom lithography

Markus K Oberthaler[1,3] **and Tilman Pfau**[2]

[1] Fachbereich Physik and Optik-Zentrum, University of Konstanz, D-78457 Konstanz, Germany
[2] 5th Institute of Physics, University of Stuttgart, D-70550 Stuttgart, Germany

E-mail: markus.oberthaler@uni-konstanz.de

Received 12 December 2002
Published 3 February 2003
Online at stacks.iop.org/JPhysCM/15/R233

Abstract
Lithography is a key technology enabling progress both in fundamental research and in widespread applications. Besides standard technologies new alternative approaches have emerged over the last few years. Here we summarize the status of the field of atom lithography where light is used to focus matter on the nanometre scale. Using the special features of the atom–light interaction a variety of structures can be produced with a spatial period limited to half the wavelength of the light. Further reduction of feature separation can be obtained utilizing the substructure of atomic matter and light polarization. Also we show how, besides various lateral structures, three-dimensional patterns can be generated in a single-step process utilizing the selectivity of the atom–light interaction.

(Some figures in this article are in colour only in the electronic version)

Contents

1. Introduction 234
2. Principle 235
3. Atom–light interaction 236
   3.1. Classical picture 236
   3.2. Quantum picture 238
   3.3. Patterning without force 242
4. Light fields as masks for atoms 242
   4.1. Aberrations 245
   Spherical aberration. 245
   Chromatic aberration. 245
   Clebsch–Gordan aberration. 245
   4.2. Possible structures 245

[3] Author to whom any correspondence should be addressed.

© 2003 IOP Publishing Ltd Printed in the UK

5. Experimental achievements 247
5.1. One-dimensional structures 247
5.2. Two-dimensional structures 248
5.3. Three-dimensional structures 250
6. Exposure technique 251
7. Other materials 252
8. Summary 253
References 254

1. Introduction

Lithography is usually discussed in the context of the semiconductor industry and Moore's law: the industry's ability to quadruple the number of transistors on a chip every three years [1]. It is the key enabler for faster and more compact computer chips [2]. The SIA roadmap 2001 already states the necessity to develop post-optical lithography technologies, while the current industrial technology still works with optical lithography using light with a wavelength of 157 nm, allowing us to realize feature widths of about 100 nm.

Besides the effort to extend optical lithography into the deep UV range at a wavelength of 13 nm other alternative lithography techniques, like electron-beam, ion-beam and x-ray lithography [3], are well developed technologies and are able to produce nanostructures with a resolution of a few nanometres. But also a few newcomers have been developed over the last few years which allow alternative routes to nanostructures. Among them are scanning probe techniques [4], imprint techniques [5], self-assembly of structures [6] and atom lithography, which will be discussed in more detail in the following. These new methods are not directly comparable to the conventional techniques as direct competitors as they come with clear disadvantages on issues like writing speed or field of view. But all of them also come with new basic features that will enable new applications to be developed, which are not easy to tackle with the standard techniques.

In this topical review we want to summarize the current status in the field of atom lithography. The main difference of this method with standard optical lithography is that the role between light and atoms is interchanged. In optical lithography light is manipulated by matter such as masks, mirrors and lenses. The structures are formed by exposing a resist and subsequent etching. The resolution is limited due to the diffraction of light. In atom lithography light acts as a mask and atoms form the pattern. The nanostructures on the surface of a substrate are either formed by the deposited atoms themselves or, in close analogy to photolithography, by using a special resist, sensitive to the atomic beam, and successive etching steps. Since atoms, whose de Broglie wavelength is only a few picometres, are imaged onto the surface, diffraction effects are currently not a limiting factor.

In the following we will discuss in detail how atom–light interaction allows us to form masks for atoms. We will elaborate on the possible nanostructures and limitations of this method. We also give a summary of experimentally achieved one-, two- and three-dimensional structures. The extension to three dimensions is a unique feature due to the material selectivity of the immaterial light masks. It allows us to write three-dimensional nanostructures in a single-step process. Since the beam is neutral and usually evaporated from an oven like, for example, in a MBE apparatus this technique is compatible with existing machines used in semiconductor physics. Finally, we give a brief overview of which atomic species this method can be applied to.

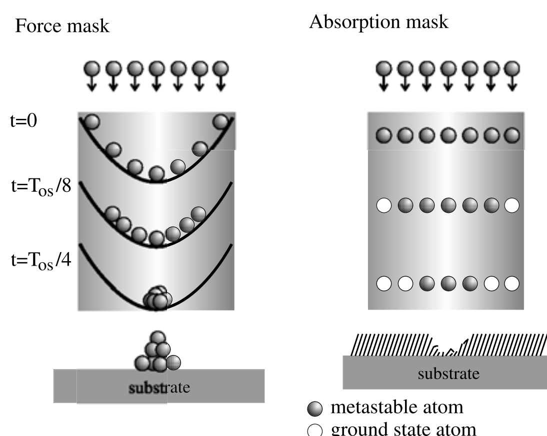

Figure 1. Two types of light masks employed in atom lithography experiments. A well collimated atomic beam impinges onto a light field. A light force mask can be described by a harmonic potential which acts like a lens for matter waves, leading to a locally enhanced growth rate on the substrate. In the case of an absorptive mask no force is present but atoms in the metastable state are pumped to the ground state except at a position where the intensity is very small. Combining this with a resist which is only sensitive to metastable atoms, due to their high internal energy, allows us to transfer this pattern onto a substrate.

2. Principle

The basic principle of atom lithography relies on the possibility of modulating the flux of an atomic beam transversally on a sub-wavelength scale utilizing the atom–light interaction. Since a modulation of the flux usually is realized by a physical mask the term 'light mask' for the light field configuration has been established over the years. Two types of light masks have been demonstrated so far which are intrinsically different in their performance (see figure 1). One kind realizes the flux modulation by locally enhancing the flux due to a spatially varying force—light force masks—while the other type reduces the flux of metastable atoms by optically pumping the atoms into the ground state—absorptive light masks for metastable atoms.

The simplest force mask is a one-dimensional harmonic potential as shown in figure 1. Since the oscillation frequency in a harmonic potential is independent of the spatial starting position the flux at the minimum of the potential is enhanced after an interaction time T_{os} corresponding to a quarter of an oscillation. Thus a harmonic potential acts like a lens for de Broglie waves, i.e. a parallel beam is concentrated at a certain point (focal point) after a certain distance (focal length). If a substrate is located in the focal plane the enhanced flux at the focal point will lead to a faster growth rate of the film locally. Therefore the substrate will reveal a topography with a local maximum at the focal point after some deposition time.

The analogy between a harmonic potential and a lens for de Broglie waves allows us to use all results on focusing properties of a lens known from photon optics to make predictions for the achievable focal spot size. In photon optics a main limiting factor is the initial divergence of the light beam. Therefore an essential prerequisite for employing force masks is the good collimation of the atomic beam (see figure 1). In experiments this is accomplished by applying the technique of transverse laser cooling.

An alternative way of producing nanostructures is followed in the case of metastable atoms where absorptive light structures can be realized. This method relies on the fact

that metastable atoms can be optically pumped to the ground state by using resonant light (i.e. optical quenching). Thus light can reduce the number of atoms in the metastable state locally, i.e. 'absorb' metastable atoms. Thus a spatially modulated atom–light interaction acts like a physical mask 'made out' of light. The resulting atomic state pattern is transferred analogously to conventional photolithography to a substrate by employing a special resist which is only sensitive to the metastable atoms due to their high internal energy (see figure 1). Using standard etching techniques allows us to transfer the resist pattern to the substrate.

3. Atom–light interaction

In this section we discuss how light can be used to manipulate the external degrees of freedom of an atom. We will concentrate on the so-called dipole force which is currently employed in atom lithography. Initially we will give a classical picture of the atom–light interaction which is sufficient to understand the ongoing physics in most of the experiments. We will also elaborate on the quantum mechanical description since some of the latest experiments can only be understood in this framework. The quantum treatment is described in the context of a two-level system but we will make clear that the extension to multi-level systems, as used in real experiments, is straightforward.

At the end we show how light can pattern an atomic beam by not exerting any force but by spatially 'absorbing' an atomic beam. We will give a short overview of possible absorptive light masks.

3.1. Classical picture

An atom interacting with near-resonant light can be modelled classically as shown in figure 2. Two mass points with opposite charge are harmonically coupled with a resonance frequency ω_0. The electric field associated with a linear polarized light field oscillates with frequency ω_l and is given by $\boldsymbol{E}(x,t) = E_0(x)\boldsymbol{e}_y\cos(\omega_l t)$ for the situation depicted in figure 2(a). This electric field leads to a driving force for the electron. The resulting dynamics of the electron is determined by the field amplitude $E_0(x)$ and the difference between the driving and resonance frequency, which is usually called detuning $\Delta = \omega_l - \omega_0$. If the detuning is much larger than the finite resonance width due to damping the resulting motion of the electron has the simple solution

$$y(x,t) = \frac{e}{2m_e\omega_l\Delta}E_0(x)\cos(\omega_l t) \tag{1}$$

where e and m_e is the electron charge and mass, respectively. Thus the electron oscillates with the driving frequency ω_l. Depending on the detuning Δ the electron oscillates either in phase with the light field ($\Delta > 0$) or out of phase ($\Delta < 0$).

Associated with the motion of the electron is a dipole moment of the atom $D(t) = -ey(x,t)$, whose local interaction energy in an electric field is given by $V(x,t) = -\boldsymbol{D}\cdot\boldsymbol{E}$. Since the induced dipole is in, or respectively out of, phase with the electric field, the atom–light interaction leads to a non-vanishing time averaged potential $V(x) = \langle -\boldsymbol{D}\cdot\boldsymbol{E}\rangle_t$. This potential governs the local motion of the atom.

Using equation (1) and the definition of the dipole moment the light induced potential (sometimes called the light potential or dipole potential) is given by

$$\langle V(x,t)\rangle_t = \frac{e^2}{4m_e\omega_l}\frac{E_0^2(x)}{\Delta} = \frac{e^2}{2c\epsilon_0 m_e\omega_l}\frac{I(x)}{\Delta} \tag{2}$$

where c is the speed of light, ϵ_0 is the dielectric constant and $I(x)$ represents the light intensity distribution. Thus we find for the blue detuned case, i.e. $\Delta > 0$, that the energy is minimal

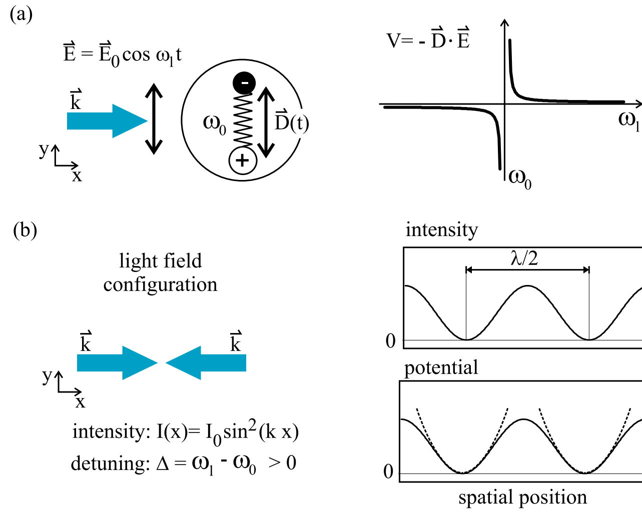

Figure 2. Classical picture for atom–light interaction. The atom is described as a positive core and a harmonically bound electron. The optical electric field with a frequency close to the resonance frequency leads to a time-dependent induced dipole moment which oscillates in (out of) phase with the driving electric field if the light field frequency is below (above) the resonance frequency. The resulting interaction energy of the induced dipole and driving field is minimized for red (blue) detuning at intensity maxima (minima). Therefore a standing light wave realized by interference of two counter-propagating light beams of wavelength λ leads to a sinusoidal potential for the atoms with a period of $\lambda/2$. This can be approximated near the nodes of the standing light wave by a harmonic potential which acts like a lens for atoms.

where the light intensity is lowest. This implies for atoms in a nonuniform light intensity distribution that they feel a force pulling them to the intensity minima where the interaction energy is minimal. Therefore in the case of blue detuning the atoms are so-called 'low field seekers'. This is in contrast to the case of red detuning, where the atoms are pulled to intensity maxima and are called 'high field seekers'.

In the following we will show that the light potential resulting from the intensity distribution of a standing light wave can be described by a spatially periodic arrangement of harmonic potentials, i.e. atomic lenses (see section 2). The light intensity of a standing light wave, which is realized by interfering two counter-propagating light beams in the x direction with wavevector $k = 2\pi/\lambda$, is given by $I(x) = I_0 \sin^2(kx)$ (see graph (b), figure 2). Assuming a positive detuning, i.e. atoms are pulled to the nodes of the standing light wave, the motion of the atoms near a node is of interest. Therefore expanding the intensity near the nodes leads to $I(x) \approx I_0 k^2 x^2$ and with equation (2) we find the harmonic potential:

$$V(x) = \frac{e^2\omega_l}{2c^3\epsilon_0 m_e}\frac{I_0}{\Delta}x^2. \tag{3}$$

Since a standing light wave has nodes with periodicity of $\lambda/2$ this light field configuration leads to a set of harmonic potentials which are separated by a distance of half the optical wavelength, as shown in figure 2.

The oscillation frequency inside these harmonic potentials and the corresponding focal length f of the atomic lens ($f = vT_{os}/4$) is given by

$$\omega_{os} = \sqrt{\frac{e^2\omega_l}{c^3\epsilon_0 m_e m}}\sqrt{\frac{I_0}{\Delta}} \qquad f = \frac{\pi v}{2\omega_{os}} \propto \sqrt{\frac{\Delta}{I_0}} \tag{4}$$

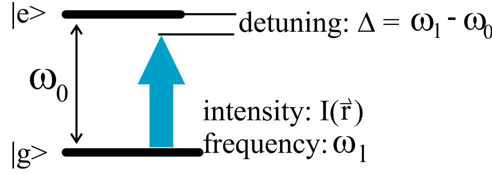

Figure 3. Two-level atom interacting with light. The internal structure is assumed to be fully described by the ground state $|g\rangle$ and the excited state $|e\rangle$. The experimental parameters which determine the atom–light interaction are the light intensity $I(\boldsymbol{r})$ and the difference between the light and atomic transition frequency, usually called detuning Δ.

where m represents the mass and v the longitudinal velocity of the atom. Since the oscillation frequency is inversely proportional to the square root of the detuning the light field has to be close to resonance in order to result in a significant force. The focal length of the atomic lenses can be estimated using typical experimental data for chromium: light power $P = 10$ mW, light beam radius $r = 100\ \mu$m, $\Delta = 2\pi \times 200$ MHz, $v = 1000$ m s^{-1}. We find $f \approx 40\ \mu$m.

It is clear that this crude model cannot predict the absolute value of the force, and thus the focal length, correctly. Therefore we will give a more rigorous quantum mechanical derivation of the force resulting from the induced dipole moment in the next section. We will find that the focal length following from equation (4) is underestimated by a factor of two. But the classical result predicts the right scaling of the focal length with the experimental parameters such as detuning Δ and intensity of the standing light wave I_0.

3.2. Quantum picture

We will now give a more rigorous quantum mechanical derivation of the dipole force. Since the general description of the atom–light interaction could be quite tedious, we will discuss a two-level atom which interacts with a classical and near-resonant light field. The interaction is described in the dipole or long wavelength approximation which assumes that the size of the atom is much smaller than the wavelength of light. The validity of this approach is well established in optical physics and documented in several books, e.g. [7].

The situation we will describe is visualized in figure 3. The corresponding Hamiltonian for a resting atom is given by

$$\hat{H} = \hat{H}_a + \hat{H}_I(t) \tag{5}$$

where $\hat{H}_a$ describes the internal states of the atom and $\hat{H}_I$ the atom–light interaction. More explicitly the Hamiltonian is given in the ground $|g\rangle$ and excited state $|e\rangle$ basis:

$$\hat{H}_a = \frac{\hbar\omega_0}{2}(|e\rangle\langle e| - |g\rangle\langle g|)$$

$$\hat{H}_I(t) = -\hat{\boldsymbol{d}}\cdot\boldsymbol{E}(\boldsymbol{r})\cos(\omega_l t) = -d_{eg}|\boldsymbol{E}(\boldsymbol{r})|\cos(\omega_l t)(|e\rangle\langle g| - |g\rangle\langle e|)$$

with $\hbar\omega_0$ as the energy difference between the ground and excited state. $\hat{\boldsymbol{d}}$ is the atomic dipole moment operator which is generally a vector operator. For the two-level atom it is given by $\hat{\boldsymbol{d}} = d_{eg}\boldsymbol{e}_\xi(|e\rangle\langle g| - |g\rangle\langle e|)$, with $d_{eg} = e\int \Psi_g^* x\, \Psi_e\, \mathrm{d}V$ and $\boldsymbol{e}_\xi$ as unit vector in the direction of the polarization of the light field. For the following discussion it is very useful to introduce the parameter $\Omega_R(\boldsymbol{r}) = \langle e|\hat{\boldsymbol{d}}\cdot\boldsymbol{E}(\boldsymbol{r})|g\rangle/\hbar$, which is called the Rabi frequency.

In order to find the potential associated with the atom–light interaction the Schrödinger equation

$$\mathrm{i}\hbar\frac{\mathrm{d}}{\mathrm{d}t}|\Psi\rangle = (\hat{H}_a + \hat{H}_I(t))|\Psi\rangle \tag{6}$$

has to be solved which is explicitly time-dependent. In order to find a simple solution one usually performs the unitary transformation $|g\rangle = e^{i\omega_l t/2}|\tilde{g}\rangle$ and $|e\rangle = e^{-i\omega_l t/2}|\tilde{e}\rangle$. This transformation leads to two terms oscillating with frequencies $\Delta = \omega_l - \omega_0$ and $\omega_l + \omega_0$, respectively. In the situations encountered in the following, the light frequencies are near resonance with the atomic transition and the intensity is low. Therefore it is an excellent approximation to ignore the rapidly oscillating terms $\omega_l + \omega_0$ [7]. This is the familiar rotating-wave approximation of atom optics and leads to a time-independent Hamiltonian which simplifies the solution of equation (6) significantly.

Finding the solution reduces to the task of calculating the eigenenergies and eigenvectors of the Hamiltonian

$$\tilde{H} = \frac{\hbar}{2}\begin{pmatrix} \Delta & -\Omega_R \\ -\Omega_R & -\Delta \end{pmatrix}. \tag{7}$$

The diagonalization of this matrix is straightforward and leads to the eigenenergies and corresponding eigenstates:

$$E_1 = -\frac{\hbar}{2}\Omega \qquad |1\rangle = \sin\theta|g\rangle + \cos\theta|e\rangle \tag{8}$$

$$E_2 = \frac{\hbar}{2}\Omega \qquad |2\rangle = \cos\theta|g\rangle - \sin\theta|e\rangle \tag{9}$$

with $\Omega \equiv \Omega(\boldsymbol{r}) = \sqrt{\Omega_R(\boldsymbol{r})^2 + \Delta^2}$ and θ defined by

$$\cos(2\theta) = -\frac{\Delta}{\Omega}, \qquad \sin(2\theta) = \frac{\Omega_R}{\Omega}. \tag{10}$$

The eigenenergies and corresponding eigenstates are depicted as a function of detuning in graph (a), figure 4. In the literature this basis is referred to as the dressed state basis. It is important to note that each basis state is a superposition of ground and excited state with relative amplitudes depending on the detuning and Rabi frequency (light intensity). Since the excited state of the atom is not stable we can distinguish between long and short lived dressed states depending on the amplitude of the excited state. For blue detuning the state $|2\rangle$ has only a small contribution of the excited state and thus represents the long living state, while for red detuning it mainly consists of the excited state and thus has a short lifetime.

The external motion of an atom in the state $|2\rangle$ is governed by the potential described by the eigenenergy E_2 which decreases with light intensity, as indicated by the dotted curve in figure 4. Thus for blue detuning an atom in state $|2\rangle$ can lower its energy by moving to lower light intensities, i.e. low field seeker. That is the same result as we have found in the classical treatment. In the case of red detuning the atom will also be attracted to the light field minimum, but for this detuning the state $|2\rangle$ is almost a pure excited state and thus has a short lifetime.

In real experiments the initial internal state of the atom is the ground state $|g\rangle$ and thus the initial state has to be described in the new basis as a superposition $|g\rangle = c_1|1\rangle + c_2|2\rangle$. For typical experimental parameters ($\Omega_R = 50\Gamma$, $\Delta = +40\Gamma0$ with Γ natural linewidth) one finds $c_1 = 0.33$ and $c_2 = 0.94$. Therefore the external dynamics of the atom is mainly given by the eigenenergy E_2 and is thus well described by the potential

$$V(\boldsymbol{r}) \approx E_2 = \frac{\hbar}{2}\sqrt{\Omega_R(\boldsymbol{r})^2 + \Delta^2}. \tag{11}$$

The resulting potential is shown in graph (b) in figure 4. For the given parameters the potential is proportional to the light intensity. For higher Rabi frequencies corresponding to higher light intensities the potential height is only proportional to the square root of the intensity.

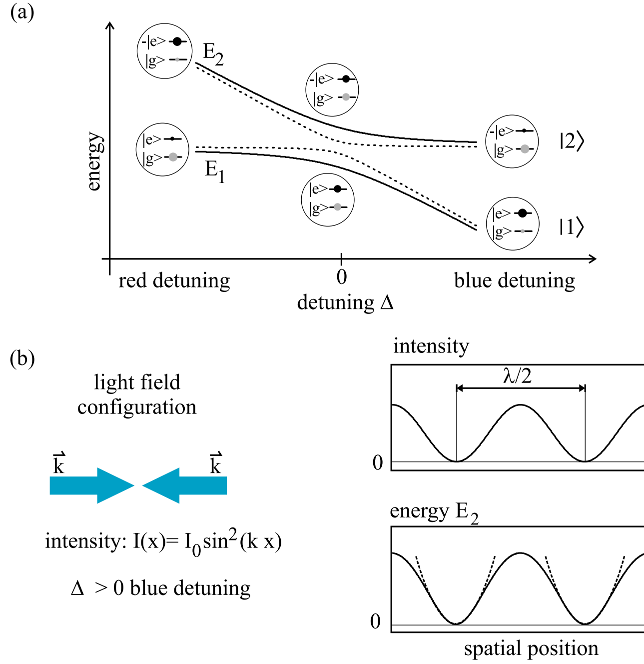

Figure 4. Graph (a) shows the eigenenergies and corresponding eigenstates of a two-level atom interacting with light. The full and dotted curves show the eigenenergies for high and low light intensity, respectively. The amplitudes of the ground and excited state are indicated by the diameter of the circles. For positive detuning the state $|2\rangle$ mainly consists of the ground state while $|1\rangle$ has a significant amplitude for the excited state and thus has a finite lifetime. The motion of a ground state atom in a blue detuned standing light wave is governed by the potential E_2 which is shown in graph (b) ($\Omega_R = 50\Gamma$, $\Delta = +40\Gamma$, where Γ represents the linewidth of the dipole transition).

The focal length can be estimated following the route described in section 3.1 equation (3). The oscillation frequency and focal length of an atom moving near the node of a standing light wave is given by

$$\omega_{os} = \Omega_R \sqrt{\frac{\omega_{rec}}{\Delta}} \qquad f = \frac{\pi v}{2\omega_{os}} \propto \sqrt{\frac{\Delta}{I_0}} \tag{12}$$

with $\omega_{rec} = \hbar k^2/2m$ (recoil frequency). For $\Omega_R = 50\Gamma$, $\Delta = +40\Gamma$ we find an oscillation frequency of 2.6 MHz, consistent with the experimental observations of a focal length of 100 μm. Note that the scaling with light intensity and detuning is the same as in the classical result.

The description so far did not include spontaneous emission due to the finite lifetime ($1/\Gamma$) of the excited state. As we will show this effect is negligible for typical atom lithography experiments in the context of force masks while this is the essential effect for absorptive light masks. The spontaneous emission rate γ_s which follows from the solution of the optical Bloch equations [8] is given by

$$\gamma_s = \frac{s_0}{1 + s_0 + (2\Delta/\Gamma)^2}\frac{\Gamma}{2} \tag{13}$$

with $s_0 = 2|\Omega_R|^2/\Gamma^2 = I/I_s$ and $I_s = \pi hc\Gamma/3\lambda^3$ the saturation intensity [8] with h Planck's constant and λ the transition wavelength. For typical experimental parameters ($\Omega_R = 50\Gamma$,

Figure 5. Eigenenergies for the multilevel chromium atom for different polarizations of the standing light field. Graph (a) represents the light intensity distribution revealing the periodicity of $\lambda/2$. In graph (b)/(c) the eigenenergies for the long living states are shown for the case of linear and circular polarization. The different potential heights are a consequence of the different Clebsch–Gordan coefficients where the square values are given in graph (d). Parameters used: $\Omega_R = 50\Gamma$, $\Delta = +40\Gamma$, $B = 0.2$ mT.

$\Delta = +40\Gamma$) one finds that about 10% of the atoms undergo a spontaneous emission event during the interaction with a 100 μm light mask, corresponding to an interaction time of 100 ns.

So far we have treated a two-level atom but in reality the ground and excited state of the atom usually have to be decomposed into magnetic substates as shown in figure 5 for the chromium $J = 3 \to 4$ transition ($^7S_3 \to {}^7P_4$). In cases of linearly (circularly) polarized light the description is straightforward since the dipole selection rules $\Delta m = 0$ ($\Delta m = \pm 1$) do not allow coupling between the magnetic sublevels of the ground state. In this situation the optical potentials can be calculated for each interacting magnetic sublevel pair in the two-level approximation taking into account the modified interaction strength due to different dipole moments d_{eg} resulting from the symmetries of the involved electronic states. The relative strengths between the different transitions are given by the Clebsch–Gordan coefficients [8], as indicated in figure 5. The light potentials for the long living states inside a standing light wave with positive detuning are given in graph (b)/(c) in figure 5. Clearly all of them exhibit the spatial periodicity of $\lambda/2$ but will lead to different focal lengths due to their different heights.

A different situation arises if the two constituting light waves are orthogonally polarized. This configuration is well known in the field of laser cooling and leads to the well known Sisyphus cooling process [9]. It is usually described as a lin $\perp$ lin configuration. Since there is no interference between the light fields the intensity distribution is constant but the polarization varies spatially from linear to circular. It is clear that the interaction energy depends on the polarization due to the Clebsch–Gordan coefficients. Circular polarization is obtained whenever the phase difference between the two orthogonal polarizations is odd multiples of $\pi/2$. This translates into a spatial period of $\lambda/4$. The period of $\lambda/8$ shown in figure 6 is a result of the coupling between the magnetic sublevels in the case of linear polarization leading to a level anticrossing and thus to new minima. This implies that the $\lambda/2$ limit of intensity light masks can be beaten by utilizing the internal structure of the atoms, as will be shown in section 5.

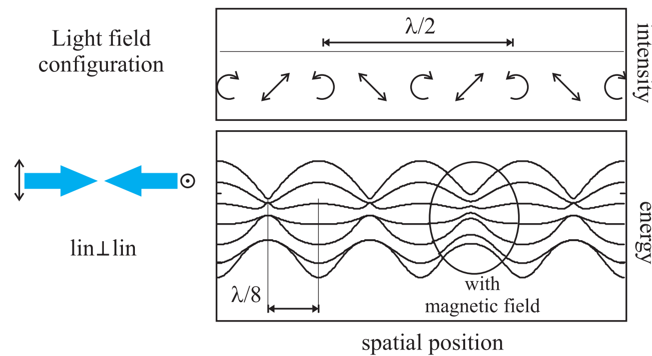

Figure 6. Eigenenergies for given light configuration of orthogonally linearly polarized counter-propagating beams. The upper graph shows the spatial variation of the polarization with a period of $\lambda/4$. The corresponding eigenenergies of the long living states are shown in the lower graph. Due to the coupling of ground state magnetic sublevels new minima are formed as a result of Raman induced anticrossing of the eigenenergies. It is important to note that the corresponding eigenstates are superpositions of all magnetic sublevels. The effect of an additional magnetic field is indicated in the inset. It allows us to separate the eigenenergies, reducing motion induced nonadiabatic transitions between the levels.

3.3. Patterning without force

The basic ingredient for this method is the use of a three-level system as indicated in figure 7. The level indicated by $|m\rangle$ is a metastable state. Since the internal energy, e.g. metastable rare gas atoms, of ~15 eV exceeds by far the kinetic energy of the atom (~0.3 eV) a resist can be found which is only sensitive to metastable atoms because enough energy for either destroying or forming the resist can be delivered (see section 6).

Therefore absorptive masks for atoms can be realized by optically pumping the atoms to the ground state. This can be experimentally implemented by light resonant with the $|m\rangle \rightarrow |e\rangle$ transition and an excited state which mainly decays into the ground state. The optical pumping rate to the excited state is given by equation (13) and reduces for low light intensities and zero detuning to

$$\gamma_p(x) = \frac{\Gamma}{2I_s} I(x). \tag{14}$$

The population ρ_{mm} of the metastable state as a function of interaction time is given by

$$\rho_{mm} = \exp\left(-\int \gamma_p(x,t)\,\mathrm{d}t\right) \tag{15}$$

where the integral is taken over the interaction time.

Thus a resonant standing light wave can pattern the atomic beam transversally with a period of $\lambda/2$ since the transmission coefficient for the metastable atoms is only one at the nodes of the standing light wave. The resulting pattern is displayed in the middle graph of figure 7. Since the optical pumping time depends also on the detuning (see equation (13)) a spatial modulation of the flux can be achieved by changing the detuning spatially as shown in graph (b), figure 7. This method is also known as frequency encoded light masks.

4. Light fields as masks for atoms

The foundation of light force masks is the concentration of the atomic flux in space due to the focusing properties of a harmonic potential. It was shown previously that using the atom–light

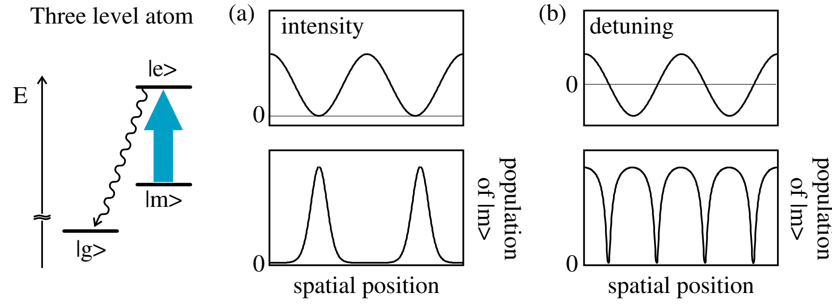

Figure 7. Absorptive masks realized with light. If light is tuned exactly on resonance with the open transition of a three-level atom (left), the atoms in the metastable state $|m\rangle$ will be optically pumped to the ground state. This optical quenching acts effectively like an absorptive mask for the metastable atoms. Lateral structuring can be achieved by changing the intensity (graph (a)) or changing the detuning (graph (b)).

interaction naturally leads to periodic sinusoidal potentials. Thus in the following discussion we focus on a potential of the form

$$V(z,x) = V_0 \exp\left(-2\left(\frac{z}{w}\right)^2\right)\sin^2(kx), \tag{16}$$

which is experimentally realized by interfering two counter-propagating Gaussian light beams with wavevector k and beam waist w. For the following discussion we assume a blue detuned light wave leading to a concentration of the atoms at the nodes of the standing light wave. The harmonic approximation in the x direction at the nodes and at $z = 0$ is

$$V(z=0,x) = V_0 k^2 x^2 = \frac{m\omega_{os}}{2}x^2 \mapsto \omega_{os} = \Omega_R\sqrt{\frac{\omega_{rec}}{\Delta}} \tag{17}$$

where Ω_R is the maximal Rabi frequency, ω_{rec} is the recoil frequency and Δ is the detuning.

There are two different ways of using these lenses, either in the thin lens regime where the focal position is outside the standing light wave or in the immersed regime where the atoms are concentrated inside the standing light wave (figure 8). In the harmonic approximation one can deduce the focal length for both types and find

$$\begin{aligned} f_{th} &= \sqrt{\frac{2}{\pi}}\frac{1}{wk^2}\frac{E_{kin}}{V_0} = \sqrt{\frac{2}{\pi}}\frac{1}{w}\frac{v^2}{\omega_{os}} \\ f_{im} &= \frac{\pi}{2k}\sqrt{\frac{E_{kin}}{V_0}} = \frac{\pi v}{2\omega_{os}} \end{aligned} \tag{18}$$

with $E_{kin} = mv^2/2$ as the kinetic energy of the impinging atoms with velocity v. Note that the immersed focal length assumes a z-independent intensity. A detailed study of the focusing properties has been performed theoretically [10] and experimentally [11]. Also two-dimensional light intensity patterns can always be harmonically expanded at the potential minima to find the focal length. For typical experimental parameters one can realize light masks with a focal length in the range of 50–100 μm.

It is important to note that for immersed focusing in the middle of a Gaussian laser beam the performance of the lens is fully described by light power and detuning. This is a consequence of the scaling of the focal length with the inverse of the Rabi frequency which is given by the square root of the light intensity. Thus for given detuning and velocity of the atom a well defined power is necessary to focus the atoms in the middle of the focused laser beam

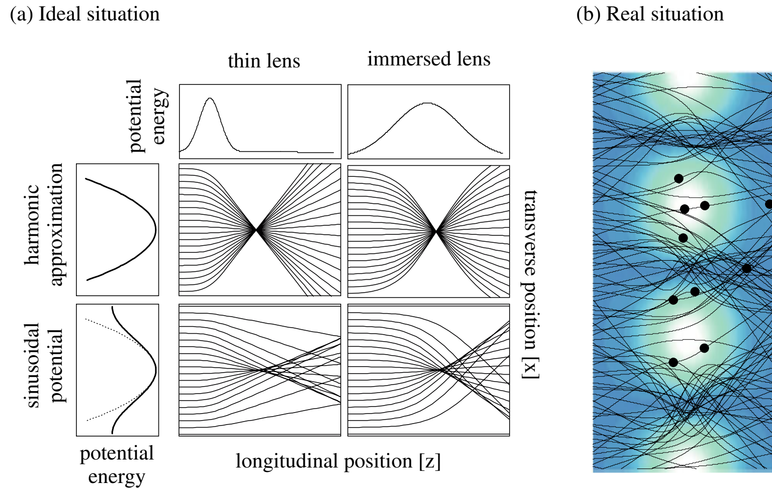

Figure 8. Graph (a) gives a comparison between thin and immersed lens focusing for harmonic and sinusoidal potentials. The left row in graph (a) summarizes the focusing properties in the thin lens regime, i.e. the atom trajectory is not significantly changed during the interaction. Clearly the trajectories in the anharmonic sinusoidal potential reveal the characteristics of spherical aberrations. The right row in graph (a) visualizes the immersed focusing regime where the focal position is inside the potential. The advantage of this type of focusing is the noncritical dependence of the focal position on the potential maximum, i.e. light intensity. Graph (b) shows the result of a simulation of the trajectories for the real situation in the experiment, taking into account all 16 magnetic sublevels, initial divergence, initial longitudinal velocity distribution and spontaneous emission (indicated with circles).

independent of the diameter of the beam. This would imply that the area of patterning can be increased without the need for more laser power. Unfortunately this scaling is not true because the spontaneous emission probability also increases with the beam diameter due to the longer interaction time. Keeping the spontaneous emission rate constant the area of patterning is proportional to the laser power.

The achievable atomic focal spot size depends on many different mechanisms. Before we discuss those mechanisms it is instructive to estimate the absolute limit, namely the diffraction limit. This can be done by applying results from photon optics [12] where the focal spot size is given by

$$d_{diff} \approx \frac{\lambda_{dB}}{2NA} \tag{19}$$

with the atomic de Broglie wavelength λ_{dB} and the numerical aperture of the lens used (standing light wave with period $\lambda/2$) given by $NA = (\lambda/2)/2f$. Assuming a thermal beam with a typical velocity of 1000 m s^{-1} and focal length of 50 μm one finds $d_{diff} \approx 2$ nm. This result shows that the observed structure widths of about 30 nm are far from this limit. Note that this result also implies that the straightforward application of this method to very slow atoms such as produced by an atom laser [13] would lead to a diffraction limited spot size bigger than the optical wavelength. A more detailed analysis has been performed by Lee [14] utilizing a quantum Monte Carlo simulation of the focusing process. His results, which also include spherical aberrations, give a limit of 8 nm.

Another limitation of the achievable structure widths is the initial divergence of the atomic beam. It is well known from photon optics that a lens focuses parallel beams onto the focal

plane. The position in respect to the optical axis depends on the angle of incidence θ and is given by

$$d_{div} = f\theta. \qquad (20)$$

Thus a divergence due to the residual transverse velocity of the atomic beam leads to a smearing out of the focal spot. In atom lithography experiments the transverse collimation is realized with laser cooling which has a natural limit and allows us to build atomic beams with a divergence of the order of $\theta \sim 0.5$ mrad, leading to focal spot sizes of about 25 nm ($f = 50$ μm).

So far we have only discussed the harmonic approximation. The real situation is depicted in graph (b), figure 8, showing simulated trajectories taking into account all 16 magnetic levels, spontaneous emission, transverse divergence and longitudinal velocity distribution. This makes clear that the real situation is far more complicated. Nevertheless one can point out some important effects leading to the observed structure widths.

4.1. Aberrations

Spherical aberration. This is a result of the anharmonicity of the sinusoidal potential and can be clearly seen in graph (a) in figure 8. Atoms not entering the light wave near the node have a slower oscillation frequency than perfectly focused atoms near the potential minimum. Thus they cross the optical axis later. Therefore those atoms are not focused and are thus responsible for a non-structured background, also called a pedestal.

Chromatic aberration. In the experiments so far thermal atomic beams with a broad longitudinal velocity distribution have been used. Since the velocity distribution is as broad as $\delta v/v \sim 1$ no simple formula can be found. A detailed numerical study by McClelland [10] shows that the velocity spread leads to a broadening from 21 to 33 nm while the main contribution to the structure width stems from the divergence of the impinging beam. The velocity dependence of the focal length (equation (18)) favours the immersed focusing technique.

Clebsch–Gordan aberration. Optical transitions usually involve magnetic sublevels. Each of those magnetic substates interact with the light, depending on the polarization (see section 3.2). In the case of chromium ($J = 3 \rightarrow 4$) the ground state is seven-fold degenerate and the Clebsch–Gordan coefficients, and thus the optical potentials, vary by more than a factor of two for linear polarization.

Summarizing one can state that, for the real experimental situation, the simple optical lens picture is not applicable but a simple numerical integration of the motion of the atoms inside the potential is possible. The result of these investigations is that the regime of immersed focusing, i.e. atoms are oscillating inside the potential and are starting to channel along the potential minima [15], is favourable. Although this does not lead to the smallest possible structures the dependence on the uncontrollable experimental parameters, such as velocity distribution, angular divergence of the beam and the Clebsch–Gordan aberration, is reduced. Thus in the experiment immersed light masks are employed.

4.2. Possible structures

So far we have described the simplest light mask which is a result of an interference of two counter-propagating light waves. It has been shown that the light intensity gradients lead to

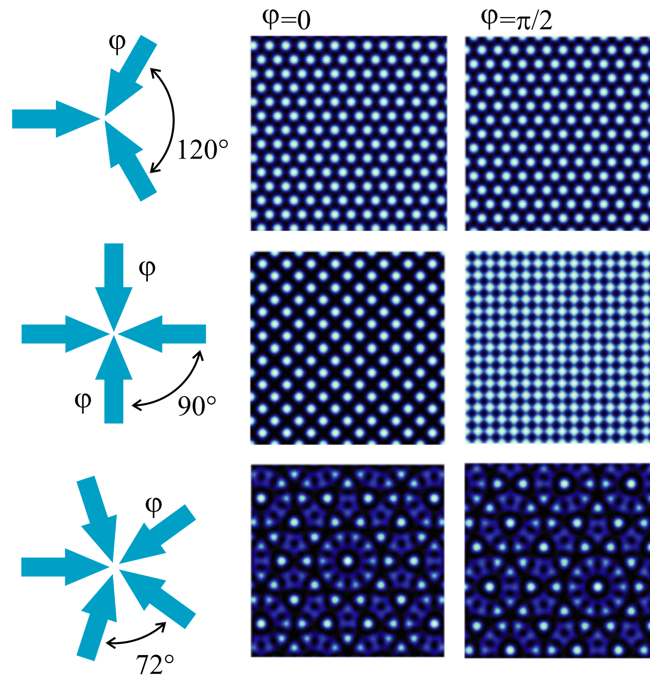

Figure 9. Two-dimensional light intensity patterns. Two-dimensional light masks can be realized by interfering more than two beams. The upper graphs show the resulting intensity pattern for a symmetric three-beam interference leading to a structure of periodically arranged intensity maxima whose symmetry does not depend on the relative phases φ between the beams. The middle line of graphs reveal that the square symmetry of a four-beam interference pattern depends on the relative phase φ between the beams. The extension to a symmetric five-beam interference pattern reveals a Penrose type structure. The lower right graph shows a general behaviour if the phase is changed in one beam only. The symmetry is preserved but spatially shifted.

forces which can concentrate the atomic flux. The most general situation is given by

$$\begin{aligned} \boldsymbol{E}(\boldsymbol{r}) &= \sum_{j=1}^{N} \boldsymbol{E}_j \mathrm{e}^{\mathrm{i}\boldsymbol{k}_j\cdot\boldsymbol{r}} \\ I(\boldsymbol{r}) &= \frac{c\epsilon_0}{2}|\boldsymbol{E}(\boldsymbol{r})|^2 = \frac{c\epsilon_0}{2}\sum_{j,l=1}^{N} \boldsymbol{E}_j \cdot \boldsymbol{E}_l^* \mathrm{e}^{\mathrm{i}(\boldsymbol{k}_j-\boldsymbol{k}_l)\cdot\boldsymbol{r}}. \end{aligned} \tag{21}$$

Obviously the general form of the intensity pattern could be very complicated but the minimal spatial period $\lambda/2$ is given by the maximal wavevector difference which is $|2\boldsymbol{k}|$. Another very important feature is the dependence of the pattern on the relative phases between the individual light waves.

A special case is the three-beam interference with maximal symmetry which is given for a relative angle between the three beams of 120°. The resulting intensity distribution reveals periodically arranged intensity maxima with a distance of $d = 2\lambda/3$. Generally one can show that, for a three-beam interference pattern, the symmetry of the intensity distribution is only given by the angles between the beams while it is independent of the relative phases between the light waves. A relative phase only shows up as a translation of the whole pattern.

This is not true for a four-beam interference pattern where the symmetry of the light field depends critically on the relative phases between the beams. As shown in figure 9 periodicity and orientation of the square lattice changes if the relative phase φ is changed by $\pi/2$.

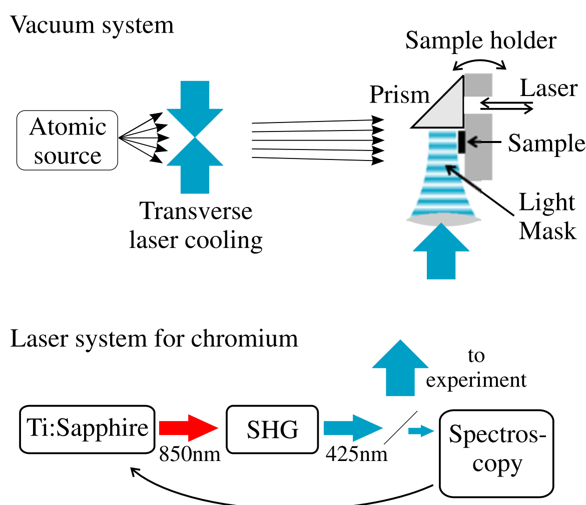

Figure 10. Experimental set-up for chromium atom lithography. The atoms are produced with an effusive source inside a vacuum chamber where the light mask is also realized. The necessary near-resonant light at 425 nm is delivered from a frequency doubled Ti:sapphire laser which is actively stabilized to the atomic transition frequency ($^7S_3 \rightarrow {}^7P_4$).

Adding more and more beams the intensity patterns become more and more complex. As an example we show the intensity pattern resulting from the interference of five light beams exhibiting a Penrose-like pattern [16].

5. Experimental achievements

The experimental data shown in the following have been achieved in the chromium experiment at Konstanz University. The experimental set-up is shown in figure 10 and represents a standard atom lithography set-up also used in other laboratories.

A laser system actively stabilized using spectroscopy delivers the necessary near-resonant laser light. The wavelength depends on the choice of the atomic transition and is, in the case of chromium, 425 nm for the $^7S_3 \rightarrow {}^7P_4$ transition. The atomic beam is realized inside a vacuum system using an effusive source leading to a beam with a divergence of a few degrees. This would lead to a washing out of the focal spot size due to the critical dependence of the focal position on the initial angle. Therefore a transverse laser cooling stage [17] is introduced leading to a beam divergence of less than 0.02°. The incident angle of the collimated beam is adjusted to within 0.1° using a right angle prism as a mirror and the reflection of a laser beam which is parallel to the atomic beam (see figure 10).

The light field, i.e. light mask, is realized directly in front of the substrate using short focal lengths for the atomic lenses. Since the focal position of a thin lens depends critically on the light power [11] immersed focusing is usually employed. After depositing a film with a thickness of 5–15 nm (≈30 min) the substrate is removed from the vacuum system and analysed using an atomic force microscope (AFM) or a scanning electron microscope (SEM).

5.1. One-dimensional structures

The first structure realized with atom lithography was produced by Timp *et al* [18] at AT&T Bell Laboratories in 1992. They used a standing light field configuration for sodium atoms

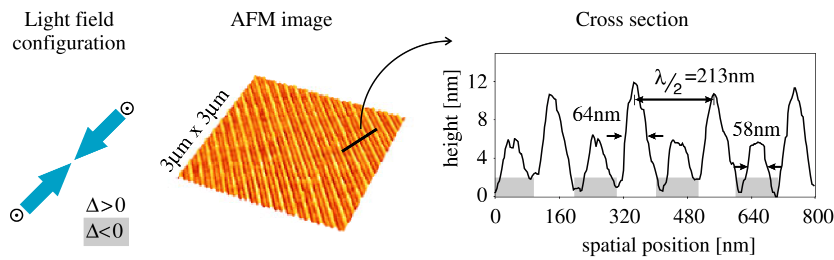

Figure 11. One-dimensional chromium structures with intensity light masks. The AFM image of the structured chromium film exhibits lines with $\lambda/4 = 106$ nm periodicity. This is a result of a double deposition through a red ($\Delta = -2\pi \times 200$ MHz, $P_{in} = 22$ mW), respectively blue ($\Delta = 2\pi \times 200$ MHz, $P_{in} = 11$ mW), detuned light mask. In the red detuned case the atoms are high field seekers and thus are concentrated at the light intensity maxima while in the blue detuned case the atoms are pushed to the nodes of the light wave.

leading to a line structure with a period of $\lambda/2 = 294$ nm. Also the smallest structure width (15 nm) achieved with atom lithography has been realized by this group [19]. Since those structures are only stable under UHV conditions, they are difficult to investigate. Additionally sodium forms droplets of 10 nm size which are statistically arranged along the line structure.

The first chromium nanostructures, which are, in contrast to sodium, stable under exposure to air, have been produced by McClelland *et al* [20] at NIST Gaithersburg using a standing light wave mask with a period of $\lambda/2 = 213$ nm. The smallest reported structure width for chromium of 28 nm has also been produced by this group [11].

How one can beat the structure period of $\lambda/2$ for intensity light masks is shown in figure 11. The structure was achieved by changing the detuning of the standing light wave from blue to red halfway through the deposition time. Since the lines are formed at the light intensity minima for positive and at the light intensity minima for negative detuning a detuning switch corresponds to moving the light mask by half the period. This leads to a line structure with a period of $\lambda/4 = 106$ nm [21, 22]. The results in figure 11 also show that the structures are strictly periodic over a range of 3 μm, demonstrating the strength of this technique to produce long range ordered structures. The periodic structures are generated over the extension of the laser and atomic beam, respectively. This corresponds to a patterned area as large as 150 μm $\times$ 3 mm.

A more elaborate method for producing one-dimensional structures with a smaller period than $\lambda/2$ is the application of polarization gradient masks (lin $\perp$ lin) as discussed in section 3.2. The technique is very atom specific but allows for chromium to reduce the structure period by a factor of four [23] and thus lead to a structure period of $\lambda/8 = 53$ nm for counter-propagating laser beams. This period can be modified by changing the angle between the light beams. In figure 12 the experimental result is shown for the light field configuration given. The angle between light beams was chosen to be 120° and the polarization is as indicated. The AFM image clearly reveals the line structure with a period of 61 nm. The period is enlarged by a factor of $2/\sqrt{3}$ in comparison with the counter-propagating light wave configuration [23] due to the angle between the light beams.

5.2. *Two-dimensional structures*

The extension of the light masks to two dimensions is straightforward. The first experiment realizing two-dimensional structures using atom lithography has employed two perpendicularly

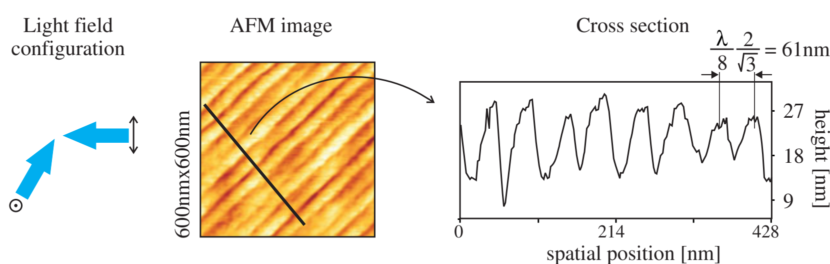

Figure 12. One-dimensional chromium structures with polarization light masks. The chosen light field configuration is shown on the left and realizes a lin $\perp$ lin polarization set-up. The observed lines reveal the reduction of the periodicity due to the new potential minima resulting from the anticrossing of energy levels due to coupling between the magnetic sublevels. The periodicity is reduced with respect to the standing light wave intensity masks by a factor of $1/2\sqrt{3}$. The experimental parameters are: $\Delta = 2\pi \times 200$ MHz, $P_{in} = 48$ mW.

arranged standing light waves. They have been polarized orthogonally such that no interference between the light beams could occur, thus realizing pure intensity gradients. This leads to a light mask with a square lattice structure and the corresponding chromium structure exhibits nanodots with 80 nm FWHM periodically arranged with a spacing of 213 nm [24].

Another configuration is the three-beam interference pattern where the angle between the beams is 120° (see section 4.2). The chromium structures achieved are shown in the upper part of figure 13. For red detuned laser light it leads to long range, periodically ordered chromium nanodots with a diameter (FWHM) of ≈100 nm and a next-neighbour distance of $2/3\lambda = 284$ nm [25]. If the laser light is blue detuned the symmetry of the structure changes to a hexagonal structure as can be seen in figure 13.

In figure 13 the results achieved with four-beam light masks are also shown. As discussed in section 4.2 the symmetry of the structure depends on the relative phases between the light beams. The realized chromium structures confirm the phase dependence of the light mask symmetry [26]. These results show that the extension to many-beam interference allows us to generate more general structures but also makes it clear that care has to be taken in stabilizing the relative phases between the beams. Similar light masks have been achieved by utilizing holograms for generating light beams coming from different directions [27]. There the relative phase of the beams is defined by the hologram. This technique opens up a new way of realizing complex light field patterns.

Two-dimensional polarization masks are also possible [28]. For the experimental demonstration the configuration as shown in figure 14 was chosen. In this configuration the polarizations of the three light beams are orthogonal (lin $\perp$ lin $\perp$ lin). This can be realized if the angle of the polarization with respect to the plane of the beams is given by $\theta = \arcsin(\sqrt{3}/2) = 35°, 25°$.

Since the interaction of a multilevel atom with these polarization gradient masks is not at all straightforward a Monte Carlo simulation [21] of the atomic trajectories was employed to predict the chromium structures. The expected pattern reveals structure widths below 20 nm which have not been confirmed experimentally. This could be a consequence of the growth process which is not yet fully understood [29]. The effect of the growth process was taken into account empirically by smoothing the simulation results with a Gaussian distribution with a standard deviation of 25 nm. The result is shown in figure 14 and shows very good agreement with experimentally obtained nanostructures.

So far we have discussed one- and two-dimensional structures which have been realized using atom lithography. Although the results show the potential of this method, in principle the

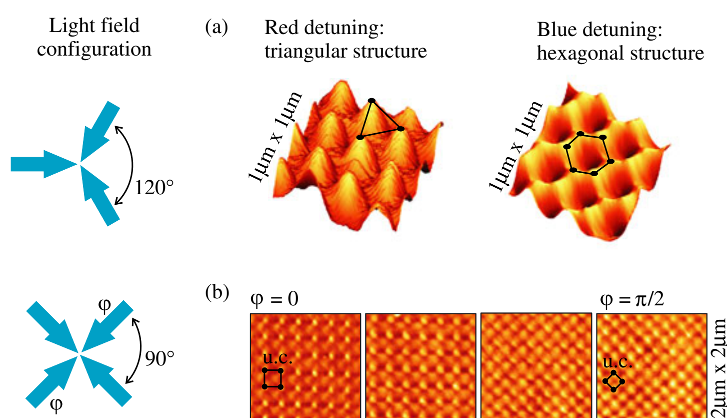

Figure 13. Two-dimensional chromium structures with three- and four-beam intensity light masks. Graph (a) shows AFM images of the chromium film topography realized with the highly symmetric three-beam interference pattern indicated at the left. In the red detuned case an array of chromium nanodots with FWHM ≈120 nm and a distance of $2\lambda/3 = 284$ nm can be produced ($\Delta = -2\pi \times 120$ MHz, $P_{in} = 7$ mW). The structure exhibits a hexagonal symmetry if the light is blue detuned ($\Delta = 2\pi \times 280$ MHz, $P_{in} = 7$ mW). Employing four-beam interference allows us to change between different symmetries of the mask by changing the relative phases between the light beams. The AFM images of the realized chromium films clearly reveal the change of the orientation and periodicity of the structure due to a phase difference between the beams.

achieved structures can be produced using standard lithography techniques. The possibility to further generalize this method to three-dimensional lithography is one of the main advantages of the technique of atom lithography.

5.3. Three-dimensional structures

In our discussion so far we have assumed that the laser is near-resonant with an atomic transition. This is necessary in order to achieve the large forces to change significantly the trajectories of the atoms within the interaction time of typically 100 ns. If the atomic beam consist of two atomic species the situation is depicted in figure 15. For the first demonstration we used a combination of chromium and magnesium fluoride, MgF_2 and the laser is tuned close to the optical transition of one species of chromium (^{52}Cr).

The chromium atoms resonantly interacting with the light are focused as discussed in the preceding paragraphs while MgF_2 is only weakly affected by the light. This allows us to realize a MgF_2 film with a laterally modulated dopant concentration of chromium [30]. The experimental set-up for the demonstration experiment is shown in graph (b), figure 15, where only an additional oven was added to the standard atom lithography set-up.

The confirmation of the successful demonstration of three-dimensional lithography has been found by utilizing the technique of Auger electron spectroscopy combined with a SEM. The results are shown in figure 16. The three-dimensional pattern was extracted by sputtering to a certain depth and then probing the surface using the Auger electron technique which only probes to a depth of less than 5 nm. Clearly one can see that, over the whole thickness of the film (≈50 nm), the ratio between the concentration of chromium and magnesium is constant, thus no de-mixing has occurred. The transverse spatial mapping of the chromium concentration 20 nm inside the sample is shown in figure 16 in graph (b). Clearly lateral modulation of the chromium concentration is observed.

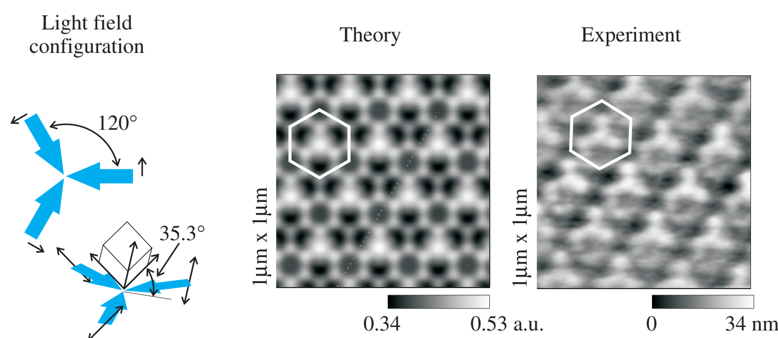

Figure 14. Two-dimensional chromium structures with a symmetric three-beam polarization light mask. Choosing the incident linear polarization with an angle of 35.3° with respect to the plane of the light mask a lin ⊥ lin ⊥ lin polarization configuration can be realized. The theoretically expected structure would reveal structure features below 20 nm. The smearing out due to the growth process was empirically included by smoothing the trajectory calculation with a spatial Gaussian filter of 25 nm width. The result describes the basic features of the observed chromium topography very well.

This technique has the advantage of being absolutely clean and can therefore be directly applied under the UHV conditions necessary for molecular-beam epitaxy, thus allowing for extension of this method to other materials. The combination of group III and V materials would allow us to grow laterally modulated heterostructures. This could open up the way to create complex three-dimensional electronic potentials, e.g. channel-like three-dimensional conductor networks.

Possibilities for producing new three-dimensional structures are indicated in graph (c), figure 15. The most straightforward way to realize three-dimensional structures is changing the flux of chromium atoms during deposition. A more elaborate change is switching between two light waves which are spatially orthogonally arranged. This leads to a wood pile structure often discussed in the context of photonic crystals [31]. A very new chiral structure so far not at all realizable (in this strictly periodic arrangement) can be produced by continuously changing the relative phases between the light masks during deposition.

6. Exposure technique

A different route to generate nanostructures with atoms utilizes the interaction between atoms and a suitable resist which is deposited in advance on the substrate.

The first resist used for atom lithography was a 1.5 nm thick self-assembled monolayer (SAM) of dodecanethiolate on a gold coated wafer [32]. The molecules form a highly ordered monolayer leading to a hydrophobic surface which protects the substrate against aqueous chemical etching solutions. Since the SAM can be damaged by impinging metastable atoms [33] or reactive atoms like caesium [34] the technique of atom lithography allows us to generate structured resists. The pattern of the resist can be transferred to the underlying gold layer by standard etching techniques. An AFM image of a gold film structured by that method is shown in figure 17. The 30 nm gold film is first covered with a dodecanthiolate SAM, then exposed to a metastable helium beam blocked by a physical mask with a cross pattern and subsequently etched [35].

This technique has been used to demonstrate absorptive light masks realized with a standing light wave. The results elucidate the Heisenberg limit of the achievable structures

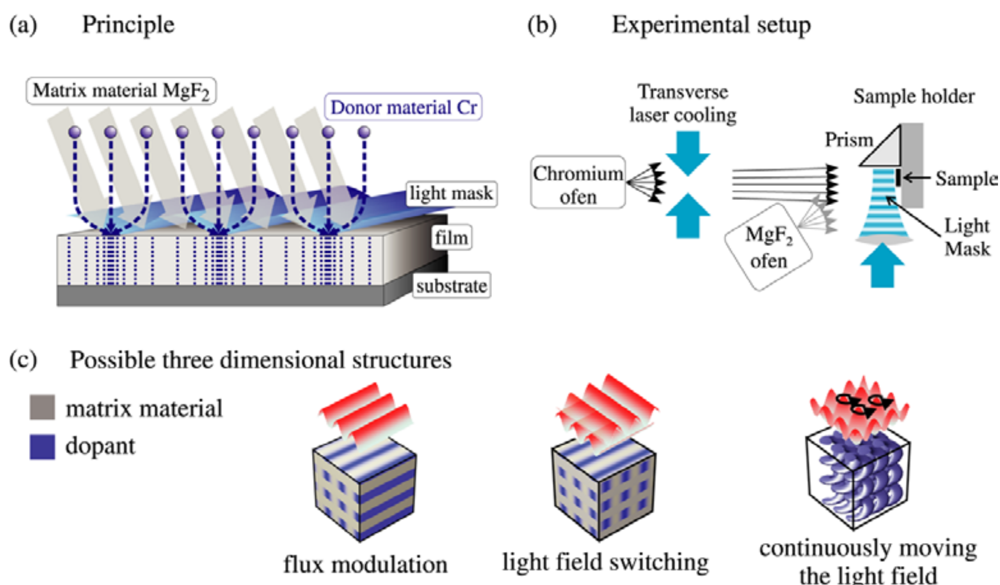

Figure 15. Three-dimensional structures realized with atom lithography. Depositing at the same time two species (Cr, MgF_2) where only one of them is resonantly interacting with light (Cr) leads to laterally structured dopant and the other species forms the matrix material. The experimental set-up is straightforward and only involves the implementation of a source producing the matrix material. Possible three-dimensional structures are given in the lower graph.

due to the wave nature of the atoms [36]. It has also been used to demonstrate focusing utilizing standing light waves with a caesium atomic beam [37] and that pulsed lasers can also be employed for lithography. This simplifies significantly the realization of high laser powers in the UV range, which is necessary for many technologically interesting atomic species [38]. Recently the frequency tuning masks as discussed in section 3.3 have also been demonstrated utilizing the exposure technique [39].

An alternative approach to destroying a SAM film by atoms is to form an etch-resistant layer due to the change in deposited background molecules on the substrate. In many set-ups diffusion pumps are connected to the experimental chambers. Thus pump oil molecules are always present as a background vapour and physisorb on the surface of the substrate. The internal energy of an impinging metastable atom can crack those molecules, leading to the formation of a carbonaceous resist. The pattern can subsequently be transferred to the substrate by using the chemical assisted ion beam etching technique [40]. Since diffusion pump oil is regarded as a contamination of the vacuum this resist is also called contamination resist. It has to be noted that this technique is well known in e-beam lithography, where it has been reported since 1964 [41].

7. Other materials

We have discussed in detail the possibilities of producing laterally nanostructured chromium films. In the following we will briefly summarize the efforts to apply this technique to other atomic species. Technologically very interesting are the group III atoms. A detailed discussion of the necessary laser wavelengths and cooling transitions can be found in [42].

The essential feature of the atom or molecule of interest is that it should have an optical transition which allows us to laser cool it. This implies that the transition is either closed

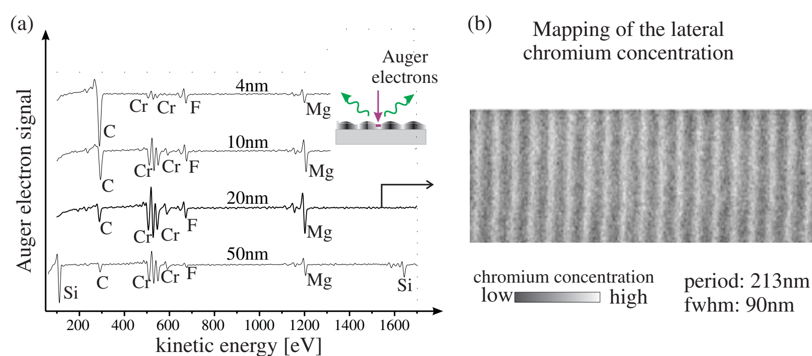

Figure 16. Confirmation of three-dimensional structures produced by the atom lithography technique. Graph (a) shows the energetically resolved Auger electron signal allowing for a spatially resolved material analysis of the sample. The depth profile was obtained by sputtering the sample and confirms that throughout the sample Cr and MgF_2 is present with the same relative concentration. Graph (b) shows the lateral mapping of the chromium concentration 20 nm inside the sample. The dopant concentration varies spatially as expected.

or can be closed by using other laser frequencies. This is essential because the achievable structure width is mainly limited by the initial beam divergence (see section 4.1). In order to maintain a reasonably high atomic flux only cooling techniques can lead to the necessary narrow divergence.

Direct deposition atom lithography has been successfully applied to sodium atoms [18], aluminium atoms [43] and chromium atoms [20]. Laser cooling of technologically interesting candidates for nanostructures are currently investigated for iron [44] and for the group III atom gallium [45]. Indium is currently under investigation if the available optical transitions allow us to create a collimated indium beam [46]. New atomic sources for direct deposition of caesium are under construction [47].

8. Summary

The technique of atom lithography has been intensively investigated over the last ten years. Many experiments have been performed since then. The main result of these experiments is that the atom–light interaction and the focusing properties of intensity light masks are well understood. Also polarization masks, which utilize the internal structure of the atoms, have been demonstrated and are well understood.

One-, two- and three-dimensional structures have been produced successfully. In particular the straightforward extension to three-dimensional structuring is a strength of this method. Another strength is the possibility of producing long range (up to mm^2) ordered periodic nanostructures with a feature size of 30 nm and period of 213 nm in the case of chromium.

Future steps will be taken in the direction of applying this method to new atomic species which are technologically interesting, such as group III atoms. Another very important step is the combination of this technique with epitaxial growth. In this context especially the growth process has to be investigated. But the successful combination of the field of epitaxial growth and atom optics will open up the way for producing new nanostructured materials with new properties.

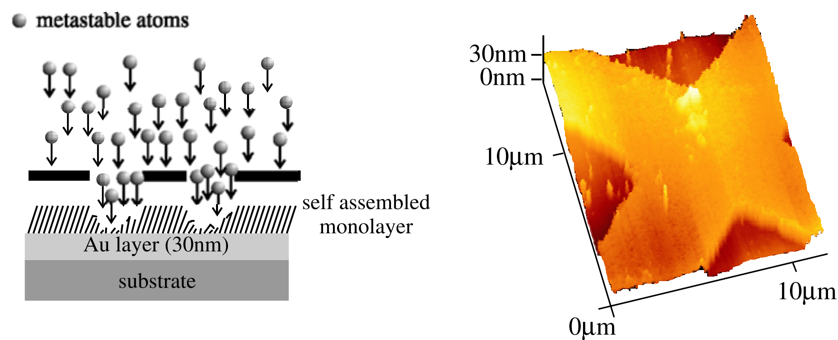

Figure 17. Exposure technique with atoms. Special resists, i.e. SAM of long molecules, are sensitive to either the internal energy of metastable atoms or the reactivity of the atoms. The flux pattern of the atomic beam leads to a modification of the resist. Subsequently the SAM pattern can be transferred to the substrate using standard etching techniques. The AFM image at the right shows a structured gold film using this technique.

References

[1] Moore G E 1965 *Elect. Mag.* **38** 114

[2] SIA Roadmap *The International Technology Roadmap for Semiconductors (ITRS)* http://public.itrs.net/

[3] Fortagne O, Kern D O and Behringer U (ed) 2001 *Proc. 26th Int. Conf. on Micro- and Nano-Engineering 2000* (Amsterdam: Elsevier)

[4] Eigler D M and Schweizer E K 1990 *Nature* **344** 524

[5] Chou S Y, Krauss P R and Renstrom P J 1995 *Appl. Phys. Lett.* **67** 3114

[6] Park M, Chaikin P M, Register R A and Adamson D H 2001 *Appl. Phys. Lett.* **79** 257

[7] Meystre P and Sargent M 1999 *Elements of Quantum Optics* (Heidelberg: Springer)

[8] Metcalf J and van der Straten P 1999 *Laser Cooling and Trapping* (New York: Springer)

[9] Dalibard J and Cohen-Tannoudji C 1989 *J. Opt. Soc. Am.* B **6** 2023

[10] McClelland J J 1995 *J. Opt. Soc. Am.* B **12** 1761

[11] Anderson W R, Bradley C C, McClelland J J and Celotta R J 1999 *Phys. Rev.* A **59** 2476

[12] Born M and Wolf E 1980 *Principles of Optics* (Oxford: Pergamon)

[13] Ketterle W 2002 *Rev. Mod. Phys.* **74** 1131

[14] Lee C J 2000 *Phys. Rev.* A **61** 63604

[15] Salomon C, Dalibard J, Aspect A, Metcalf H and Cohen-Tannoudji C 1987 *Phys. Rev. Lett.* **59** 1659

[16] See [21]
Experiment for realization is under construction
Jurdik E 2002 private communication

[17] Drewsen M, Drodofsky U, Weber C, Maus C, Schreiber G and Mlynek J 1996 *J. Phys. B: At. Mol. Opt. Phys.* **29** L843
Scholten R E, Gupta R, McClelland J J, Celotta R J, Levenson M S and Vangel M G 1997 *Phys. Rev.* A **55** 1331

[18] Timp G, Behringer R E, Tennant D M, Cunningham J E, Prentiss M and Berggren K K 1992 *Phys. Rev. Lett.* **69** 1636

[19] Behringer R E, Natarajan V and Timp G 1997 *Opt. Lett.* **22** 114

[20] McClelland J J, Scholten R E, Palm E C and Celotta R J 1993 *Science* **262** 257

[21] Brezger B 1999 *PhD Thesis* University of Konstanz

[22] Schulze Th, Brezger B, Schmidt P O, Mertens R, Bell A S, Pfau T and Mlynek J 1999 *Micro. Eng.* **46** 105

[23] Gupta R, McClelland J J, Marte P and Celotta R J 1996 *Phys. Rev. Lett.* **76** 4689

[24] Gupta R, McClelland J J, Jabour Z J and Celotta R J 1995 *Appl. Phys. Lett.* **67** 1378

[25] Drodofsky U, Stuhler J, Schulze Th, Drewsen M, Brezger B, Pfau T and Mlynek J 1997 *Appl. Phys.* B **65** 755

[26] Schulze Th, Brezger B, Mertens R, Pivk M, Pfau T and Mlynek J 2000 *Appl. Phys.* B **70** 671

[27] Mützel M, Tandler S, Haubrich D, Meschede D, Peithmann K, Flaspöhler M and Buse K 2002 *Phys. Rev. Lett.* **88** 83601

[28] Brezger B, Schulze Th, Schmidt P O, Mertens R, Pfau T and Mlynek J 1999 *Europhys. Lett.* **46** 148

[29] Jurdik E, Rasing Th, van Kempen H, Bradley C C and McClelland J J 1999 *Phys. Rev.* B **60** 1543

Bradley R M, Eschmann A and Lee S A 2000 *J. Appl. Phys.* **88** 3316
See also [11]
[30] Schulze Th, Müther T, Jürgens D, Brezger B, Oberthaler M K, Pfau T and Mlynek J 2001 *Appl. Phys. Lett.* **78** 1781
[31] Joannopoulos J D, Villeneuve P R and Fan S 1997 *Nature* **386** 143
[32] Berggren K K, Bard A, Wilbur J L, Gillaspy J D, Helg A G, McClelland J J, Rolston S L, Phillips W D, Prentiss M and Whitesides G M 1995 *Science* **269** 1255
[33] He: see [35]
Ar: see [32]
Ne: see
Engels P, Salewski S, Levsen H, Sengstock K and Ertmer W 1999 *Appl. Phys.* B **69** 407
[34] Kreis M, Lison F, Haubrich D, Meschede D, Nowak S, Pfau T and Mlynek J 1996 *Appl. Phys.* B **63** 649
Berggren K K, Younkin R, Cheung E, Prentiss M, Black A, Whitesides G M, Ralph D C, Black C T and Tinkham M 1997 *Adv. Mater.* **9** 52
[35] Nowak S, Pfau T and Mlynek J 1996 *Appl. Phys.* B **63** 203
[36] Johnson K S, Thywissen J H, Dekker N H, Berggren K K, Chu A P, Younkin R and Prentiss M 1998 *Science* **280** 1583
[37] Lison F, Adams H J, Haubrich D, Kreis M, Nowak S and Meschede D 1997 *Appl. Phys.* B **65** 419
[38] Mützel M, Haubrich D and Meschede D 2000 *Appl. Phys.* B **70** 689
[39] Thywissen J and Prentiss M 2002 *Preprint* org/abs/physics/0209084
[40] Rehse S J, Glueck A D, Lee S A, Goulakov A B, Menoni C S, Ralph D C, Johson K S and Prentiss M 1997 *Appl. Phys. Lett.* **71** 1427
[41] Broers A N 1964 *Proc. 1st Int. Conf. on Electron and Ion Beam Science and Technology* ed R Bakish (New York: Wiley) p 191
[42] Rehse S J, McGowan R W and Lee S A 2000 *Appl. Phys.* B **70** 657
[43] McGowan R W, Giltner D M and Lee S A 1995 *Opt. Lett.* **20** 2535
[44] te Sligte E, Bosch R C M, Smeets B, van der Straten P, Beijerinck H C W and van Leeuwen K A H 2002 *Proc. Natl Acad. Sci.* **99** 6509
[45] Rehse S J, Fairbank W M Jr and Lee S A 2001 *J. Opt. Soc. Am.* B **18** 855
[46] Meschede D 2002 private communication
[47] Camposeo A, Piombini A, Cervelli F, Tantussi F, Fuso F and Arimondo E 2001 *Opt. Commun.* **200** 231